Fluid Dynamics & Materials Processing

Tech Science Press

DOI: 10.32604/fdmp.2023.029427

ARTICLE

Simulation of Moving Bed Erosion Based on the Weakly Compressible Smoothed Particle Hydrodynamics-Discrete Element Coupling Method

Qingyun Zeng[1,2], Mingxin Zheng[1,*] and Dan Huang[2]

[1]School of Transportation Engineering, East China Jiaotong University, Nanchang, 330000, China

[2]School of Architectural and Art, Jiangxi Industry Polytechnic College, Nanchang, 330000, China

[*]Corresponding Author: Mingxin Zheng. Email: zhengmingxin0317@yeah.net

Received: 18 February 2023 Accepted: 05 May 2023 Published: 27 October 2023

ABSTRACT

A complex interface exists between water flow and solid particles during hydraulic soil erosion. In this study, the particle discrete element method (DEM) has been used to simulate the hydraulic erosion of a granular soil under moving bed conditions and surrounding terrain changes. Moreover, the weakly compressible smoothed particle hydrodynamics (WCSPH) approach has been exploited to simulate the instability process of the free surface fluid and its propagation characteristics at the solid–liquid interface. The influence of a suspended medium on the water flow dynamics has been characterized using the mixed viscosity concept accounting for the solid–liquid mixed particle volume ratio. Numerical simulations of wall-jet scouring and reservoir sediment flushing on a mobile bed were performed and validated with experiments. The results show that the proposed WCSPH–DEM coupling model is highly suitable for determining parameters, such as the local maximum scour depth, the scour pit width, and the sand bed profile. The effects on the hydraulic erosion process of two important parameters of the mixed viscosity coefficient (initial solid volume concentration and initial viscosity coefficient) are also discussed to a certain extent in this study.

KEYWORDS

Hydraulic soil erosion; WCSPH-DEM coupling model; suspended medium; mixed viscosity coefficient

1 Introduction

Typical hydraulic soil erosion, such as runoff erosion and overtopping erosion, usually occur when water flows through loose rivers, subgrade slopes, earth-rock dams, and other structures. These occurrences have raised concerns about the mechanism of hydraulic soil erosion and the intensity of its activity, which are primarily studied through physical model tests. Numerous experimental results have shown that hydrodynamic scour damage is mainly caused by the vortex and submerged flow [1,2], and is broadly divided into three stages; initial scour, scour pit development, and scour depth balance [3]. The scale and intensity of scouring activity are predicted using empirical or semi-empirical formulas derived from relevant model tests. Some examples are the formula proposed by Xue et al. [4] for calculating the overtopping erosion depth of an earth-rock dam and the formula derived by Zhao et al. [5] for calculating the maximum scour depth of debris flow. However, the model test has a scale effect, and it struggles to

accurately and comprehensively capture the process of development of the scoured bed as well as the flowfield information of the sand-carrying flow [6,7].

Numerical methods are increasingly being used for accurate refined analysis and to predict the trend of development of the water–soil coupled contact process. The most important aspect of the numerical simulation of hydraulic soil erosion is the treatment of the moving interface between the solid and liquid phases [8]. Coupled continuum–discrete methods are ideal for modeling hydraulic soil erosion behavior; particulate matter in a fluid is modeled by discrete elements, whereas the fluid is modeled as a continuum governed by constitutive laws [9]. The discrete element method (DEM) and element-free Galerkin (EFG) (EFG, improved DEM) method, which are used to determine general behavior through interaction laws in small-scale particle assembly, are ideal tools for granular systems [10,11]. Many continuum approaches such as the finite volumes method (FVM), finite difference method (FDM), and lattice Boltzmann method (LBM), have been coupled to the DEM or EFG to characterize the interaction of heterogeneous fluids with moving granular soils [12–15]. However, in mesh-based methods (e.g., FVM, FDM, and LBM), tedious meshing is required to track the position of the moving solid–liquid interface when dealing with the coupled contact problem of the solid–liquid two–phase flow. Moreover, on a fixed mesh element, the free surface, deformation boundary, and moving interface may struggle to define some defects accurately [16]. Although the DEM and EFG are highly effective for analyzing the deformation of contact between soil particles as well as between soil particles and structures, it is difficult to use these methods directly for obtaining the non-physical parameters (such as friction coefficient and elastic modulus) of the solid–liquid contact zone through experiments. Consequently, it is impossible to accurately describe the stress–strain behavior of solid particles in the liquid phase [17]. For the coupled contact analysis involving multi-phase flow, DEM and EFG methods based on geotechnical mechanics should be coupled with hydrodynamic methods.

Recently, the smoothed particle hydrodynamics (SPH) method proposed by Gingold et al. [18] in 1977 has rapidly advanced. The SPH method uses Lagrangian particles to discretize the continuous spatial computational domain. These particles carry physical quantities (such as mass, density, and velocity) that characterize the behavior of the computational domain. Thus, the method easily determines the contact interface between different materials and is suitable for simulating interface changes caused by hydraulic erosion [19–21]. Ma et al. [22] established the SPH solid–liquid two-phase flow model based on the Oldroyd-B constitutive governing equations and the modified Shields criterion, and they simulated the sediment transport and erosion on the free surface. Padova et al. [23] used the weakly compressible SPH and two-dimensional turbulence model to study the mechanism of the vortex formation of downstream hydraulic erosion. Ng et al. [24] proposed an SPH scheme, which is a coupled Newtonian viscosity equation and Hersch-Bulkley-Papanasasiou (HBP) non-Newtonian control equation. The SPH scheme was used to describe the solid–liquid contact of the two-phase flow, and the feasibility of the method was verified through a simulation of wave erosion on bank sediment. Although the SPH method can adequately characterize the flow pattern changes and soil deformation during hydraulic soil erosion, the hydrodynamics motion governing model inaccurately describes the stiffness degradation and strength reduction of solid soil particles [25]. Therefore, SPH has been coupled with DEM to investigate the behavior of scouring between fluids and solids and to fully characterize the nonlinear properties of interactions between soil particles. For example, Abbas et al. [26] used the one-way coupling of the weakly compressible SPH (WCSPH) method and the DEM to show the additional circulating sediment transport mechanism in front of the vertical breakwater, as well as its direct impact on the bed surface sediment scour scale. Iwamoto et al. [27] introduced the SPH-DEM coupled model based on the local average equation of motion to explore the breakwater instability and failure mechanism caused by the tsunami erosion of the soil behind the breakwater. To improve the computational efficiency and numerical stability of the conventional SPH-DEM model, Kim et al. [28] proposed an improved ISPH-CGDEM

model and verified the applicability of the coupled model through three hydraulic soil erosion simulation cases.

However, these studies are limited to the clear water erosion of particles and do not fully consider the change in flow properties caused by suspended particles during erosion. Bed particles typically undergo different states from static to dynamic during erosion, and some particles remain suspended at the bottom of the flow, causing moving bed erosion. Hence, the single-phase SPH method considers the use of elastoplastic or viscoelastoplastic constitutive equations to describe the motion of solid–liquid two-phase flow [29,30]. However, existing control equations of the SPH-DEM model often only assume the viscosity coefficient of water flow as a constant and do not adequately characterize the dynamic change in water flow properties. Therefore, researchers should dynamically modify the coupling control variables of the SPH-DEM model and explore the influence of suspended bed particles on the erosion morphology of the moving bed.

This paper presents a WCSPH-DEM coupling model for modeling hydraulic soil erosion. First, the flow control equation and coupling mechanism of the WCSPH-DEM model are introduced. Unlike the traditional method, the mixed viscosity coefficient of water flow that characterizes the influence of suspended bed particles is combined with water-sediment contact calculation. Subsequently, two hydraulic soil erosion cases are considered for numerical simulation, and the simulation results are compared with the experimental results. The verified WCSPH-DEM model is then applied to explore the influence of the mixed viscosity coefficient on hydraulic erosion morphology. Finally, we present the conclusion and prospects of the coupling strategies adapted in the current research.

2 Numerical Model

The focus of this study is the complex interface interaction between water flow and soil particles in hydraulic soil erosion. The SPH method based on Lagrange description as well as the DEM method based on Newton's second law interpolation is used to establish a coupling model. The model comprises three main parts: a water flow model based on the N-S equation; a soil deformation and failure model based on bond contact relationship; and a water-soil interface interaction and erosion model.

2.1 Governing Equations

Solid–liquid two-phase flow is often involved in hydraulic soil erosion. Owing to the large difference in the soil particle sizes, the contact flow around soil particles is prone to velocity difference, forming shape resistance; friction resistance also exists between solid particles. The control equation of a weakly compressible fluid under the Lagrangian framework does not consider the resistance term caused by differences in solid particles. Therefore, the combined drag force of shape resistance and friction resistance, and the buoyancy caused by particle volume drainage are introduced as the control components of momentum exchange and energy balance between continuous flow and discontinuous soil particles [28,31,32].

The governing equations (mass and momentum conservation equations) of a weakly compressible fluid, considering the coupling of two-phase flow, can be expressed as follows [28,32]:

$$\frac{d\rho_f}{dt} + \rho_f \nabla \cdot \boldsymbol{u}_f = 0, \tag{1}$$

$$\rho_f \frac{d\boldsymbol{u}_f}{dt} = \nabla \cdot \boldsymbol{\sigma} - \boldsymbol{fd}_f - \boldsymbol{fb}_f + \rho_f \boldsymbol{g}, \tag{2}$$

where ρ, $\boldsymbol{u}$, $\boldsymbol{\sigma}$, and $\boldsymbol{g}$ represent density, velocity component, total stress tensor, and gravity component, respectively. $\boldsymbol{fd}_f$ and $\boldsymbol{fb}_f$ denote the drag force and buoyancy of the fluid element, respectively. ∇ is the divergence symbol.

The motion characterization of a solid particle satisfies the following equation [32]:

$$\rho_s \frac{d\boldsymbol{u}_s}{dt} = -\nabla P + \boldsymbol{fd}_s + \boldsymbol{fc}_s + \rho_s \boldsymbol{g} + \boldsymbol{fb}_s, \tag{3}$$

where P is pressure; $\boldsymbol{fd}_s$, $\boldsymbol{fc}_s$, and $\boldsymbol{fb}_s$ represent the drag force on the solid particle, interaction forces between solid-phase particles, and buoyancy exerted by the fluid on the solid particle, respectively. The subscripts f and s refer to fluid elements and solid particles, respectively.

2.2 Fluids Governed by SPH

Hydraulic soil erosion has a complex flow pattern, and the shallow-water equation does not accurately reflect scouring flow characteristics. The discrete modification of the mass and momentum conservation equations is often used to characterize the motion of particle flow. Thus, the governing equations of weakly compressible fluids in the Lagrangian framework can be written as follows [32–34]:

$$\frac{d\rho_i}{dt} = \sum_{j=1}^{N} m_j u_{ij}^{\alpha} \frac{\partial W_{ij}}{\partial x_i^{\alpha}}, \tag{4}$$

$$\frac{du_i^{\alpha}}{dt} = g^{\alpha} + \sum_{j=1}^{N} m_j \left(\frac{\boldsymbol{\sigma}_i^{\alpha\beta}}{\rho_i^2} + \frac{\boldsymbol{\sigma}_j^{\alpha\beta}}{\rho_j^2} \right) \frac{\partial W_{ij}}{\partial x_i^{\beta}} - \frac{Fd_{s\to f,i}^{\alpha} + Fb_{s\to f,i}^{\alpha}}{m_i}, \tag{5}$$

where x_i^{α} and $u_{ij}^{\alpha} = u_i^{\alpha} - u_j^{\alpha}$ represent the position vector and velocity vector, respectively; α and β denote the Cartesian components x, y, z; $\boldsymbol{\sigma}_i^{\alpha\beta}$ is the total stress tensor of SPH particles; $Fd_{s\to f,i}$ and $Fb_{s\to f,i}$ represent the drag force and buoyancy force exerted by DEM particles on SPH particle i, respectively; subscript i, j indicates an arbitrary SPH (fluid) particle.

The kernel function W_{ij} determines the performance of the SPH simulation; it not only determines the interpolation accuracy of the SPH approximation, but is also related to the numerical stability. In this paper, the cubic spline kernel function is used as follows:

$$W(R,h) = \begin{cases} \alpha_d \left(\frac{2}{3} - R^2 + \frac{1}{2}R^3 \right), 0 \le R < 1 \\ \frac{\alpha_d}{6}(2-R)^3, 1 \le R < 2 \\ 0, R \ge 2 \end{cases}, \tag{6}$$

where $\alpha_d = \frac{15}{7\pi h^2}$ and $\frac{3}{2\pi h^3}$ represent the 2D and 3D spatial distributions of SPH particles, respectively, $\left|\boldsymbol{r}_{ij}\right| = \left|\boldsymbol{x}_i - \boldsymbol{x}_j\right| = L_0$, $R = \left|\boldsymbol{r}_{ij}\right|/h$. As the smoothing length h of the particle decreases, its radius of action decreases, reducing the number of interpolation iterations and saving computer memory. However, Wu et al. [35] found that as the smooth length decreases, the constraint force in the SPH particle influence domain decreases, which easily causes numerical interruption. Accordingly, $L_0 < h \le 1.5\ L_0$ should be satisfied between the initial particle spacing L_0 and the smoothing length h for a sufficient number of correlated particles in the influence range, which ensures the convergence of the calculation results [35].

The total stress tensor can be decomposed into an isotropic normal stress P and a shear stress tensor $\boldsymbol{\tau}^{\alpha\beta}$:

$$\boldsymbol{\sigma}^{\alpha\beta} = -P\delta^{\alpha\beta} + \boldsymbol{\tau}^{\alpha\beta}, \tag{7}$$

where $\boldsymbol{\delta}^{\alpha\beta}$ is the Kronecker delta. When $\alpha = \beta$, $\boldsymbol{\delta}^{\alpha\beta} = 1$; otherwise, $\boldsymbol{\delta}^{\alpha\beta} = 0$.

When we consider the effect of suspended particles, they are generally regarded as a mixture of water and particles; their internal flow resistance is expressed by viscous shear stress and obtained from the material model [31]. The heterogeneous water is modeled using the Bingham model [36,37]:

$$\boldsymbol{\tau}^{\alpha\beta} = 2\mu_{eff} \cdot \dot{\varepsilon}^{\alpha\beta} = 2\left(\frac{\boldsymbol{\tau}_y}{|\dot{\gamma}|} + \mu_0\right)\dot{\varepsilon}^{\alpha\beta}, \tag{8}$$

where μ_{eff} and μ_0 represent effective viscosity and plastic viscosity coefficient, respectively; $\boldsymbol{\tau}_y$ represents yield strength, which controls the flow state before fluid instability failure and satisfies the Mohr–Coulomb yield criterion.

For a weakly compressible fluid, $\dot{\varepsilon}^{\alpha\beta}$ is the shear strain rate tensor and can be described by the following vector expression based on the velocity gradient [25,38]:

$$\dot{\varepsilon}^{\alpha\beta} = \dot{\varepsilon}_{xy}\boldsymbol{i} + \dot{\varepsilon}_{yz}\boldsymbol{j} + \dot{\varepsilon}_{xz}\boldsymbol{k}, \tag{9}$$

$$\text{In which } \dot{\varepsilon}_{xy} = \dot{\varepsilon}_{yx} = \frac{1}{2}\left(\frac{\partial u_x}{\partial y} + \frac{\partial u_y}{\partial x}\right), \dot{\varepsilon}_{yz} = \dot{\varepsilon}_{zy} = \frac{1}{2}\left(\frac{\partial u_z}{\partial y} + \frac{\partial u_y}{\partial z}\right), \dot{\varepsilon}_{xz} = \dot{\varepsilon}_{zx} = \frac{1}{2}\left(\frac{\partial u_x}{\partial z} + \frac{\partial u_z}{\partial x}\right); \tag{10}$$

$$\begin{aligned} u^{\alpha} &= (u_x, u_y, u_z)^T \qquad x^{\alpha} = (x, y, z)^T \\ u^{\beta} &= (u_y, u_z, u_x)^T, \qquad x^{\beta} = (y, z, x)^T. \end{aligned} \tag{11}$$

Then, $\dot{\varepsilon}^{\alpha\beta}$ is simplified by Cartesian components:

$$\dot{\varepsilon}^{\alpha\beta} = \frac{1}{2}\left(\frac{\partial u^{\alpha}}{\partial x^{\beta}} + \frac{\partial u^{\beta}}{\partial x^{\alpha}}\right). \tag{12}$$

In the above expression, the discrete expression for the shear strain rate $\dot{\varepsilon}_i^{\alpha\beta}$ of arbitrary particle i in SPH can be written in the following form:

$$\dot{\varepsilon}_i^{\alpha\beta} = \left.\frac{\partial u^{\alpha}}{\partial x^{\beta}}\right|_i = \frac{1}{2}\left(\sum_{j=1}^{N}\frac{m_j}{\rho_j}\left(u_j^{\alpha} - u_i^{\alpha}\right)\frac{\partial W_{ij}}{\partial x_i^{\beta}} + \sum_{j=1}^{N}\frac{m_j}{\rho_j}\left(u_j^{\beta} - u_i^{\beta}\right)\frac{\partial W_{ij}}{\partial x_i^{\alpha}}\right), \tag{13}$$

where u^{α} is the velocity component, and the SPH discrete form of its velocity gradient satisfies the mass conservation criterion. $|\dot{\gamma}|$ is the shear rate which can be defined as

$$|\dot{\gamma}| = \sqrt{2\dot{\varepsilon}^{\alpha\beta}\dot{\varepsilon}^{\alpha\beta}} = \sqrt{2\left[\left(\frac{\partial u^{\alpha}}{\partial x^{\alpha}}\right)^2 + \left(\frac{\partial u^{\beta}}{\partial x^{\beta}}\right)^2 + \frac{1}{2}\left(\frac{\partial u^{\alpha}}{\partial x^{\beta}} + \frac{\partial u^{\beta}}{\partial x^{\alpha}}\right)^2\right]}. \tag{14}$$

Among the commonly used rheological models, the Bingham model [39] reflects the linear relationship between the shear rate and shear stress of the fluid after yielding. In a stable state, when the shear rate $|\dot{\gamma}|\to 0$, the shear stress is equal to the yield stress. However, according to Eq. (8), the shear rate cannot be zero in the Bingham model. To avoid the singularity of the flow model at the boundary of the numerical calculation domain, the regularized Bingham equation [40] is introduced as follows:

$$\mu_{eff} = \frac{\tau_y}{|\dot{\gamma}|}\left(1 - \boldsymbol{e}^{-m|\dot{\gamma}|}\right) + \mu_0 = \frac{\tau_y}{\sqrt{\varepsilon_{\Pi}}} + \mu_0, \tag{15}$$

where ε_{Π} is the second invariant of the shear strain tensor, and m is a regularized constant. Eq. (15) shows that when $|\dot{\gamma}|\to 0$, the fluid is about to enter the plastic deformation stage, and its initial viscosity is close to the viscosity coefficient when the fluid yields. At this time, the shear stress can be approximated to the yield

stress. However, when m is infinite, the approximate solution $m\tau_y + \mu_0$ of the effective viscosity is extremely large, easily causing a result overflow. Therefore, to ensure computational efficiency and accuracy, m is usually taken in a small order of magnitude (100–1000) [41].

Soil particles at a water–soil coupling interface are suspended at the bottom of the water flow by the scouring and buoyancy of water, increasing the viscosity of the bottom water flow. The increased viscosity directly affects the dynamic characteristics of the two-phase interface and influences the calculation results. Therefore, the effective viscosity coefficient should be modified to consider the influence of suspended particles on the flow properties. The most common method is to track the change in the solid–liquid volume concentration in the water flow containing suspended particles, after which the effective viscosity coefficient is amplified by an exponential function [38,42]. Therefore, the mixed viscosity coefficient of flow containing suspended particles satisfies:

$$\mu_{mix} = \begin{cases} \mu_{eff} e^{\dfrac{2.5\alpha_s}{1 - 39\alpha_s/64}}, \alpha_s \le 0.3 \\ \mu_{eff}, \alpha_s > 0.3 \end{cases} \tag{16}$$

where α_s is the volume ratio of solid particles (sediment volume fraction) in the affected flow zone, and its discrete calculation formula is

$$\alpha_{s,i} = \sum_{k_{sat} \in 2h}^{N} \frac{m_k}{\rho_k} \Big/ \sum_{k \in 2h}^{N} \frac{m_k}{\rho_k}, \tag{17}$$

where k_{sat} is a solid particle that satisfies the erosion initiation condition in the influence domain of particle i; h is the smooth length. The influence domain of SPH particles on DEM particles can be determined by referring to the water–soil coupling interface treatment method proposed by Manenti et al. [43] (as shown in Fig. 1). The $2h$ depth range at the coupling interface is the potential erosion area (exposed soil particles), and the DEM particles beyond the $2h$ depth range are regarded as part of the fixed boundary (hidden soil particles).

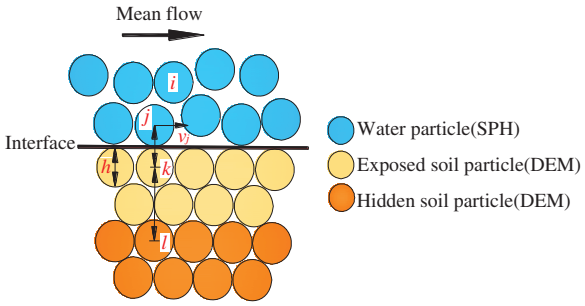

Figure 1: Water-sediment contact interface diagram

In this paper, we refer to the contact treatment between the suspended medium and the boundary in the mechanics of sediment motion [38,42]. When $\alpha_s \le 0.3$, the water erosion occurs in the exposed soil particles layer, and the mixed viscosity is applied to calculating the relative motion of the mixed medium. When $\alpha_s > 0.3$, the suspended medium is considered to have reached the interface between the exposed soil particles layer and the hidden soil particle layer. At this time, the contact between the suspended medium and the fixed boundary particles is calculated by the effective viscosity.

In the SPH method for weakly compressible fluid problems, the motion of water particles is produced by the pressure gradient. Therefore, the dynamic pressure change in the particle calculation domain can be corrected by the SPH state equation in weak compression form [44]:

$$P_i = B\left[\left(\frac{\rho_i}{\rho_0}\right)^{\lambda} - 1\right], \tag{18}$$

where $B = c_0^2\rho_0/\lambda$; $\lambda = 7$. ρ_0 and ρ_i represent the original density (base density) and liquid density of the fluid in the SPH particle calculation domain, respectively. c_0 is the artificial sound velocity, and, generally, $c_0 \geq 10u_{\max}$, where $u_{\max}$ represents the maximum velocity in the fluid flow process.

The SPH control equations (Eqs. (4) and (5)) are solved using the liquid phase coupling of the state equation (Eq. (18)) and the stress–strain equation (Eq. (7)), and the rheological model of the flow with suspended particles is established.

2.3 DEM Description of Soil Particles

The DEM is a molecular-dynamics-based numerical simulation method developed by Cundall et al. [10], and it was first applied to the problem of discontinuous media in rock mechanics. The fundamental concept of the DEM is the expression of discontinuous points through discrete particles; Newton's second law and time step iteration are then used to solve the motion control equations of the discrete particles, obtaining the overall motion form of the discontinuous points.

We simulated the solid particles under hydraulic scouring using spherical DEM particles. The motion includes two kinds of six degrees of freedom; translational and rotational, which are mainly controlled by force and moment. The force of solid particles is usually dominated by the contact force between particles as well as the force between particles and the water flow medium.

Meanwhile, natural sand grains are not spherical. Hence, we used the rotational moment to reduce the inhomogeneity of the soil particles and simulate the tumbling of the particles by changing the angle [28]. Overall, the governing equations satisfying the translation and rotation of DEM particles are as follows:

$$\frac{\partial u^{\alpha}_{dem,k}}{\partial t} = \frac{Fd^{\alpha}_{f\to s,k} + Fb^{\alpha}_{f\to s,k} + Fc^{\alpha}_{kl}}{m_k} + g^{\alpha}, \tag{19}$$

$$I_k\frac{\partial \omega_k}{\partial t} = Tc_{kl}, \tag{20}$$

where Fc_{kl} is the solid interparticle force; $Fd_{f\to s,k}$ and $Fb_{f\to s,k}$ represent the resistance and buoyancy of the liquid on the solid particle k, respectively, and are the main forces driving the movement of the solid phase particles caused by the fluid medium, as defined in Section 2.3. $I_k = m_k d_k^2/10$ represents the moment of inertia, d_k is the particle diameter, ω_k is the rotational speed, and Tc_{kl} is the interaction torque. Subscript k, l indicates an arbitrary DEM particle.

Fig. 2 illustrates the mechanical model of the interaction between DEM particles [10]. When two DEM particles collide, the contact force Fc_{kl} can be decomposed into the normal and tangential directions, represented by the local coordinates between the particles. The specific contact force equation is

$$Fc_{kl} = Fc^n_{kl} + Fc^s_{kl}, \tag{21}$$

where the contact force component in the normal direction Fc^n_{kl} and the contact force component in the tangential direction Fc^s_{kl} satisfy [45,46]

$$Fc^n_{kl} = K^n \cdot \Delta x^n + \eta^n \Delta u^n, \tag{22}$$

$$Fc_{kl}^{s} = \begin{cases} K^{s} \cdot \Delta x^{s} + \eta^{s} \Delta u^{s}, \left|Fc_{kl}^{s}\right| \le \mu \left|Fc_{kl}^{n}\right| \\ \mu \left|Fc_{kl}^{n}\right| \Delta u^{s} / \left|\Delta u^{s}\right|, \left|Fc_{kl}^{s}\right| > \mu \left|Fc_{kl}^{n}\right| \end{cases}, \tag{23}$$

in which μ is the static friction coefficient between DEM particles. K, Δx, η, and Δu are the elastic coefficient, relative displacement, viscous damping coefficient, and relative velocity, respectively. When the tangential component of the contact force satisfies $\left|Fc_{kl}^{s}\right| > \mu \left|Fc_{kl}^{n}\right|$, the DEM particles slide at the contact point.

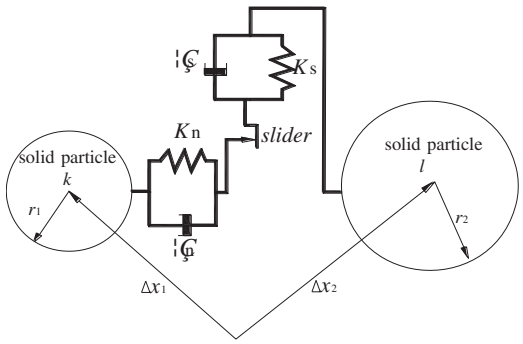

Figure 2: Diagram of contact between solid particles in the DEM model

Additionally, the displacement and rotation of particles can be tracked in the movement of DEM particles. Through the first-order Taylor expansion of the increment of velocity and angular velocity, we derive the iterative calculation equations for displacement and angle at each time step:

$$\left(u_k^{\alpha}\right)_{t+\frac{\Delta t}{2}} = \left(u_k^{\alpha}\right)_{t-\frac{\Delta t}{2}} + \left(\frac{\partial u_k^{\alpha}}{\partial t}\right)_t \cdot \Delta t, \tag{24}$$

$$\left(x_k^{\alpha}\right)_{t+\Delta t} = \left(x_k^{\alpha}\right)_t + \left(u_k^{\alpha}\right)_{t+\frac{\Delta t}{2}} \cdot \Delta t, \tag{25}$$

$$\left(\omega_k\right)_{t+\frac{\Delta t}{2}} = \left(\omega_k\right)_{t-\frac{\Delta t}{2}} + \left(\frac{\partial \omega_k}{\partial t}\right)_t \cdot \Delta t, \tag{26}$$

$$\left(\theta_k\right)_{t+\Delta t} = \left(\theta_k\right)_t + \left(\omega_k\right)_{t+\frac{\Delta t}{2}} \cdot \Delta t. \tag{27}$$

2.4 WCSPH-DEM Coupling Model

During hydraulic soil erosion, the interaction between the solid and liquid phases is related to the power transfer and energy dissipation between various media. Therefore, we propose a two-phase flow coupling model based on the contact forces (drag force and buoyancy) between the particle DEM component and SPH component (as shown in Fig. 3), and we applied the model to the solid–liquid SPH-DEM simulation.

The drag force is related to the solid–liquid friction velocity, the density of distribution of DEM particles in the influence range of SPH particles, and the volume of DEM particles. In view of the change in the flow properties caused by suspended particles under water erosion, we replace the original clear water viscosity coefficient with the modified mixed viscosity coefficient in the SPH-DEM coupling model. In reference to the two-fluid calculation model [32,46], the drag force of SPH particles on DEM particles satisfies

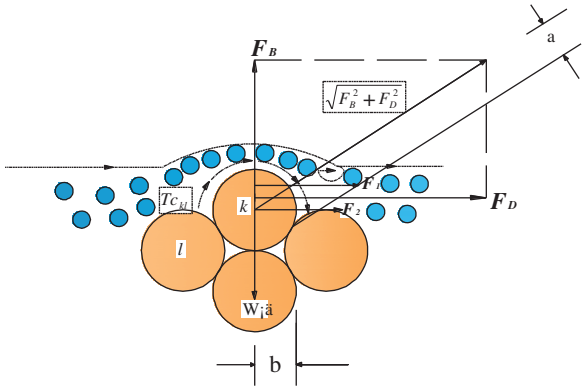

Figure 3: Contact force and torque of fluid particles acting on solid particles

$$Fd^{\alpha}_{f\to s,k} = \left(\bar{u}^{\alpha}_{sph,k} - u^{\alpha}_{dem,k}\right)\cdot V_k \cdot \zeta_k, \tag{28}$$

$$\zeta_k = \begin{cases} 150\dfrac{1-\varepsilon_k}{\varepsilon_k}\cdot\dfrac{\mu_{mix,f}}{d_k^2} + 1.75\dfrac{\rho_f}{d_k}\left|\bar{u}^{\alpha}_{sph,k} - u^{\alpha}_{dem,k}\right|, \varepsilon_k \le 0.8 \\ 0.75C_d\cdot\dfrac{\rho_f}{d_k}\cdot\varepsilon_k^{-1.65}\left|\bar{u}^{\alpha}_{sph,k} - u^{\alpha}_{dem,k}\right|, \varepsilon_k > 0.8 \end{cases}, \tag{29}$$

$$\varepsilon_k = \frac{\sum_{k\in dem} W_{ik}V_k}{\sum_{k\in dem,sph} W_{ik}V_k}, \quad \bar{u}^{\alpha}_{sph,k} = \frac{\sum\limits_i u_i^{\alpha} W_{ik}V_i}{\sum\limits_i W_{ik}V_i}, \tag{30}$$

where $\bar{u}^{\alpha}_{sph,k}$ is the average velocity of SPH particles around DEM particles, and V_k is the volume of DEM particles. ε_k is the local porosity, which depends on the unit volume density of DEM particles. To make the calculated local porosity continuous in space, the smooth length h should be at least 2 times larger than the median diameter of DEM particles [47]. The fluid resistance coefficient ζ_k is defined by the equations of Ergun [48] and Wen et al. [49] to meet different particle porosity conditions.$\mu_{mix,f}$, d_k, and ρ_f represent the mixed viscosity coefficient, DEM particle diameter, and fluid density, respectively. C_d is the drag coefficient of DEM particles, which satisfies the following expression [50]:

$$C_d = \begin{cases} \dfrac{24}{R_e}(1 + 0.15{R_e}^{0.681}), R_e \le 1000 \\ 0.42, R_e > 1000 \end{cases}, \tag{31}$$

$$R_e = \frac{\left|\bar{u}^{\alpha}_{sph,k} - u^{\alpha}_{dem,k}\right|\cdot\varepsilon_k\rho_f\cdot d_k}{\mu_{mix,f}}, \tag{32}$$

where R_e is the DEM particle Reynolds number, and $\left|\bar{u}^{\alpha}_{sph,k} - u^{\alpha}_{dem,k}\right|$ is the friction velocity.

In the case of an extremely low friction velocity, the variance can be neglected, and the drag is mainly caused by the friction of the liquid acting on the surface of the particle. When the friction velocity increases gradually, the streamlines on the DEM particle surface are separated, the pressure difference is generated before and after, and the shape resistance is finally developed [31]. Therefore, the general form of the drag force can be defined by the resultant force of surface friction F_1 and shape resistance F_2.

Buoyancy is also a crucial contact force in the SPH-DEM coupling model and is usually characterized by fluid pressure gradient under the control of state equation [27,32]:

$$Fb_{f\to s,k} = V_{dem,k}\nabla P_{sph,i}\left(x_i^{\alpha}\right) = V_k \sum_i \frac{m_i p_i}{\rho_i}\cdot\frac{\partial W_{ik}}{\partial x_i^{\alpha}}. \tag{33}$$

However, for the analysis of the solid–liquid two-phase flow under water erosion, the influence of suspended particles on fluid properties cannot be ignored. Therefore, we introduce the mixed viscosity coefficient $\mu_{mix,f}$ and average velocity $\bar{u}_{sph,k}^{\alpha}$ to increase the buoyancy calculation term under the action of suspended particles:

$$\begin{aligned} Fb_{f\to s,k} &= V_{dem,k}\left(\nabla P_{sph,i}\left(x_i^{\alpha}\right) + \mu_{mix,f}\nabla^2\bar{u}_{sph,k}^{\alpha}\right) \\ &= V_k\left(\sum_i V_i\cdot P_i\cdot\frac{\partial W_{ik}}{\partial x_i^{\alpha}} + \mu_{mix,f}\cdot\sum_i\left(V_i\cdot\bar{u}_{sph,k}^{\alpha}\cdot\frac{\partial^2 W_{ik}}{\partial\left(x_i^{\alpha}\right)^2} + V_i^2\cdot\bar{u}_{sph,k}^{\alpha}\left(\frac{\partial W_{ik}}{\partial x_i^{\alpha}}\right)^2\right)\right). \end{aligned} \tag{34}$$

Because Newton's third law governs the interaction forces, the drag force and buoyancy of the DEM particle on the SPH particle are of the same magnitude as that of the reaction of the DEM object on the SPH fluid, but in opposite directions.

2.5 Operation Process of the Coupled Model

A fixed time step is used in the DEM and SPH modules, and the calculation time step should be less than the critical time step; otherwise, the calculation will not converge. The critical time step of solid particles (Δt_s) in the DEM model can be controlled by the normal elastic coefficient K^n of DEM particles, and is expressed as [51]:

$$\Delta t_s = \frac{2\pi}{5}\sqrt{m_k/K^n}. \tag{35}$$

The critical time step for the SPH module (Δt_f) is usually determined by the Courant-Friedrichs-Lewy (CFL) condition [52]:

$$\Delta t_f = CFL\cdot\min(\Delta t_w, \Delta t_{cv}), \tag{36}$$

$$\Delta t_w = \sqrt{\frac{h}{|\boldsymbol{a}_i|_{\max}}}, \qquad \Delta t_{cv} = \frac{h}{\max(c_0, 10|\boldsymbol{u}_{\max}|)}, \tag{37}$$

where $|\boldsymbol{a}_i|_{\max}$ and $|\boldsymbol{u}_i|_{\max}$ denote the maximum acceleration and maximum velocity on SPH particles, respectively; CFL is the Courant number, and $CFL = 0.1$ was selected in the hydraulic erosion research.

Owing to the differences in material properties and algorithms, the values of critical time steps Δt_s and Δt_f are largely different, and Δt_s is usually smaller than Δt_f. In addition, the SPH method is an interpolation algorithm, and the value of Δt_f is insufficiently large, which affects the calculation efficiency and the accuracy of the results. To synchronize the operation of the SPH and DEM models, we optimized and integrated the multi-time step operation program. Fig. 4 describes the computational process of the SPH-DEM program.

3 Model Validation

We investigated the validity and accuracy of the SPH-DEM coupling model in simulating hydraulic soil erosion. A water storage depth h = 0.15 m (as illustrated in Fig. 5) was used for the simulation according to the wall-jet scouring and reservoir sediment flushing experimental model designed by Khanpour et al. [53]. First, for the wall-jet test, a 0.15 m high water flow was stored in a 0.2 m × 0.7 m flume, and the flume gate

was designed to be lifted quickly by 0.05 m to form a water jet. The fine sediment riverbed (0.085 m × 0.45 m, d_{50} = 0.85 mm) was set in the downstream of the flume. The arrival of the discharge flow induced the hydraulic soil erosion. Second, for the reservoir sediment flushing test, a 0.15 m × 1 m dense sedimentary sand layer (d_{50} = 0.85 mm) was tiled at the bottom of the storage tank, which was 0.05 m higher than the downstream riverbed. As the water storage depth of the upper part of the sedimentary sand layer reached 0.15 m, the gate was quickly opened to initiate the erosion of the sediment layer by the burst water flow.

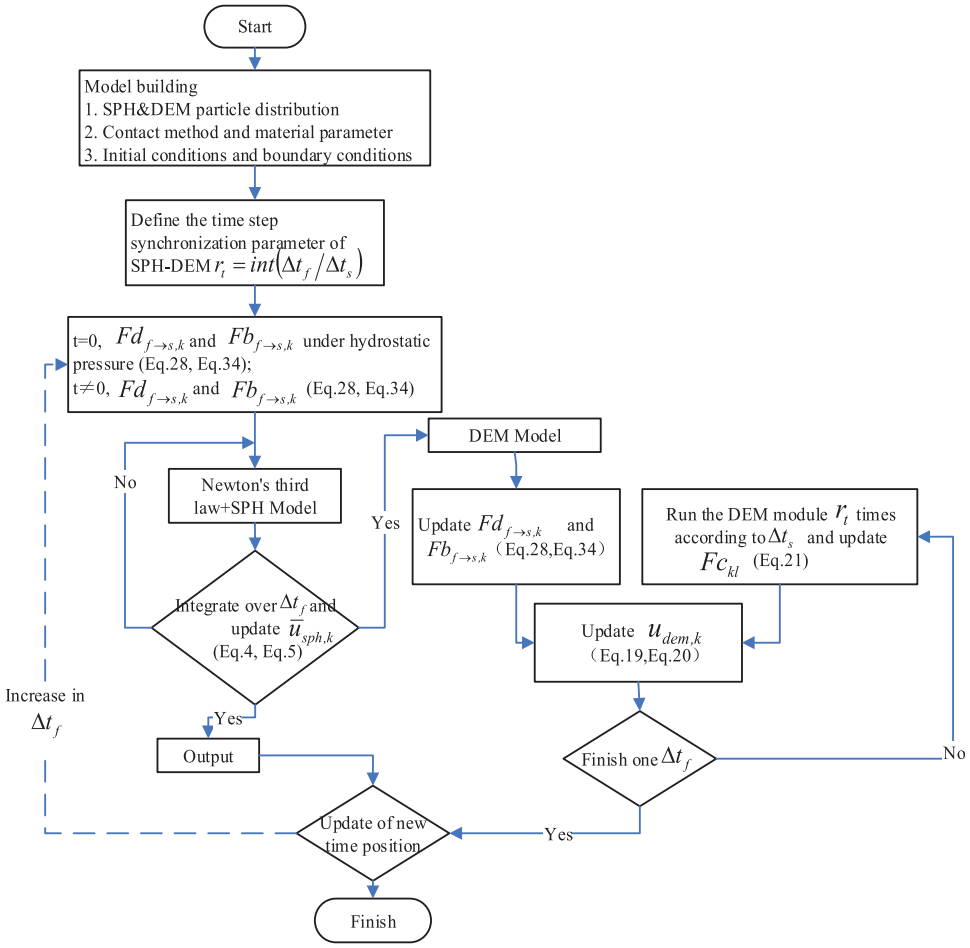

Figure 4: Simplified flow chart representation of the procedure for one time step of the coupled SPH-DEM model

Considering the different aspects of the solid–liquid two-phase flow, we used SPH discrete particles to represent the stored water flow in the simulation process and DEM particles to define the sediment. NULL material was used for the liquid unit as the material shares similar parameters with water. Solid particles were assigned by the PLASTIC_KINEMATIC material to ensure that they have the same density, elastic modulus, and Poisson's ratio as those of natural sand. The NULL material was also used to replace the test groove and gate made of smooth glass, whereas SPH particles with rigid constraints were used to characterize the boundary, satisfying the calculation criteria of the boundary particle method [54]. The weakly compressible SPH state equation was selected for the motion control and dynamic pressure balance of the water flow. The initial stress state, boundary conditions, and model size of the SPH-DEM numerical model established in the simulation were consistent with those of Khanpour's experiment [53]. Table 1 presents the material properties of the reservoir flushing and wall-jet scouring caused by a dam break.

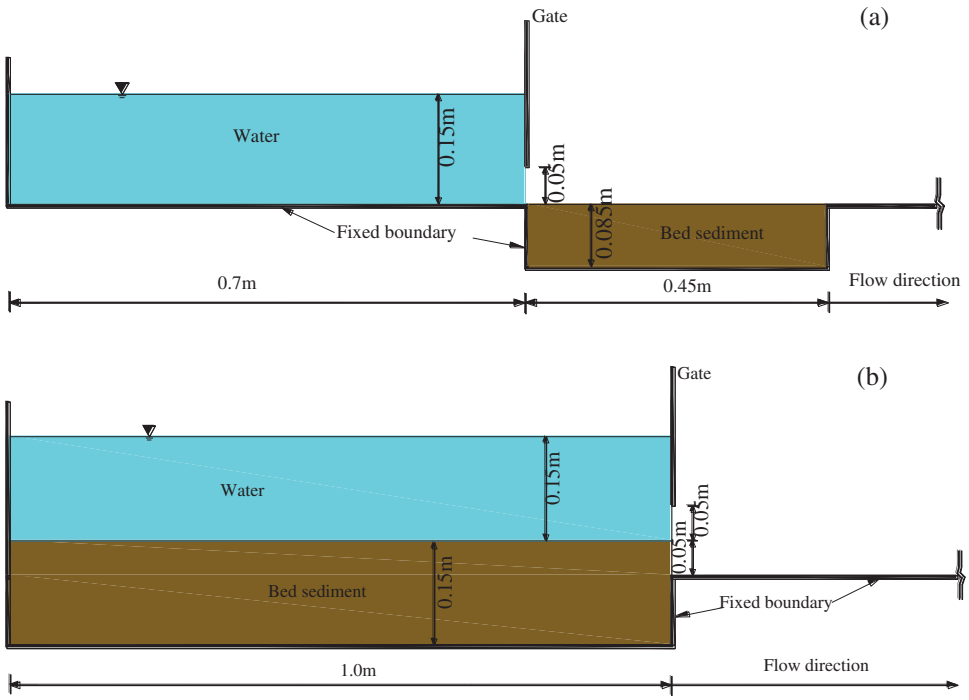

Figure 5: Two-dimensional schematic of the model tests for (a) sediment scouring and (b) reservoir sediment flushing

Table 1: Material models and parameters for simulating hydraulic soil erosion

Parameters	Symbol	Value	Reference
Boundary	Young's modulus (GPa)	200	[54]
	Poisson ratio	0.25	
	Density (kg/m^3)	7850	
Water phase	Sound velocity c_0 (m/s)	1480	[53]
	Initial density ρ_0 (kg/m^3)	1000	[53]
	The constant λ	7	[53]
	Dynamic viscosity μ_0 (Pa.s)	0.001	[53]
Sediment phase (natural sand)	Young's modulus (MPa)	100	[28]
	Poisson ratio v	0.3	[28]
	Grain density ρ_s (kg/m^3)	2650	[53]
	Initial porosity ε_k	0.66	[53]
	Friction coefficient μ	0.6	[53]
	Elasticity coefficient in both normal and tangential directions K^n, K^s (N/m)	10^3	[32]
	Damping coefficient in both normal and tangential directions η^n, η^s	0	[32]

3.1 Test 1: Sediment Scouring Caused by Wall-Jet Flow

To simulate the behavior of the erosion of the downstream bed sand caused by a wall-jet flow, we established a coupled SPH-DEM simulation model (see Fig. 6). The liquid SPH particles were filled into a groove with a width of 0.7 m, length of 0.1 m in the paper direction, and height of 0.15 m. The solid DEM particles in the downstream sediment layer were distributed randomly. For the movable sediment layer, 85350 DEM particles (d_{50} = 0.85 mm) were used, satisfying the initial porosity of 0.66. Water particles and boundary particles were placed at the same particle spacing of 5.0 mm, yielding 40500 SPH particles and 8250 fixed SPH particles, respectively.

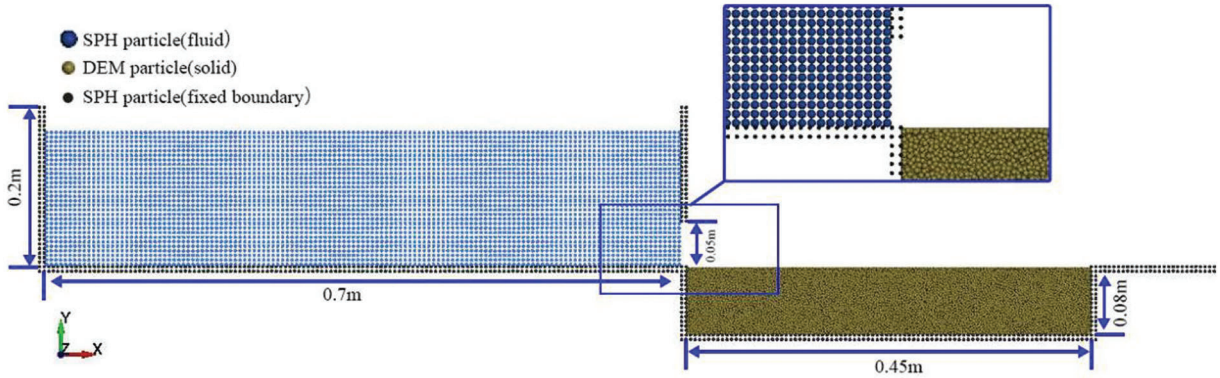

Figure 6: Two-dimensional schematic of the SPH-DEM coupling model

To verify the applicability of the SPH-DEM coupling model, we compared the numerical results with the experimental results (Fig. 7). The simulated solid–liquid two-phase flow pattern is highly consistent with that of the experiments. The profile of the bed sediment after erosion at different time nodes is consistent with the profile observed in the model experiment. Fig. 8 illustrates the velocity distribution when the dam-break flow erodes the downstream sand bed. As shown in the refined area of Figs. 8b and 8c, the shallow DEM particles have obvious erosion entrainment under the action of SPH particles, and according to the velocity distribution gradient, a layer of suspended DEM particles is formed at the solid–liquid interface. As shown in Fig. 8d, the wall-jet is squeezed and accumulated at the gate, and the free surface in the reservoir is turbulent, forming reverse waves. As the reverse waves develop, the flow velocity of SPH particles at the outlet gradually decreases. Consequently, the downstream liquid level hump turns reverses direction (see Figs. 8e and 8f), causing turbulence in the suspended DEM particle layer at the solid–liquid interface. The overlap between SPH particles and DEM particles is due to the visualization of SPH particles which has no effect on the simulation [46].

As shown in Fig. 8b, nonphysical splashing of SPH particles occurs in the refined area, and similar cases have been reported in other SPH-based calculations [35,55]. Bakti et al. [55] reported that changes in the density of SPH particles near the boundary are more obvious than those of other regions because of boundary constraints, which considerably enlarge the density discontinuity of boundary particles and the calculation complexity. At the moment of contact of some SPH particles, the interaction force exceeds the constraint force in the particle influence domain, resulting in nonphysical splashing of particles. In addition, the smooth length h is small (h = 1.05 L_0 in this study), and the constraint force of the SPH particle influence domain is relatively small [35], which also facilitates particle splashing. However, with the gradual release of pressure, the nonphysical splash of the particles disappears (see Figs. 8e and 8f). Compared with the experimental results, the simulation results show that the slight nonphysical particle splash of the current particles has little effect on the calculation results.

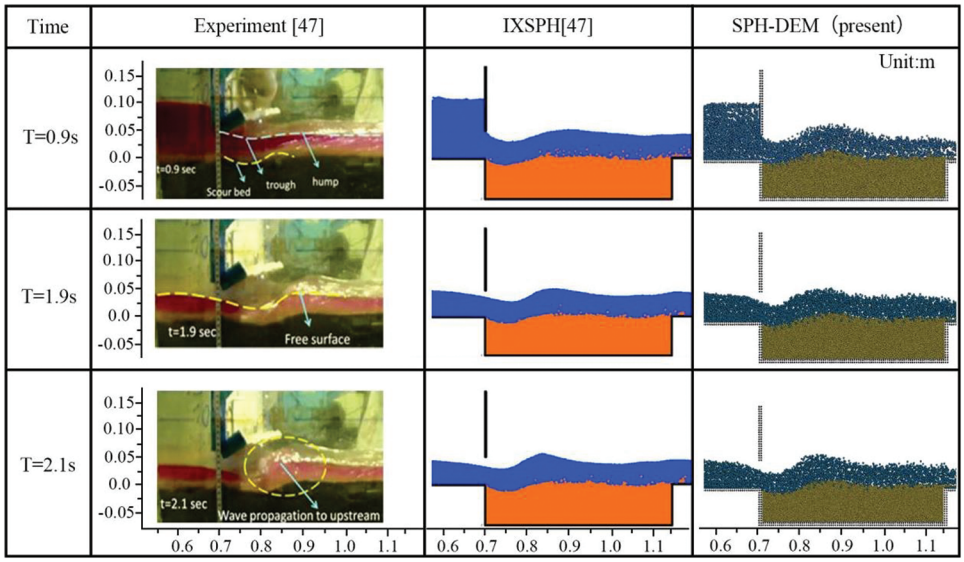

Figure 7: Experimental and numerical results of the wall-jet scouring experiment

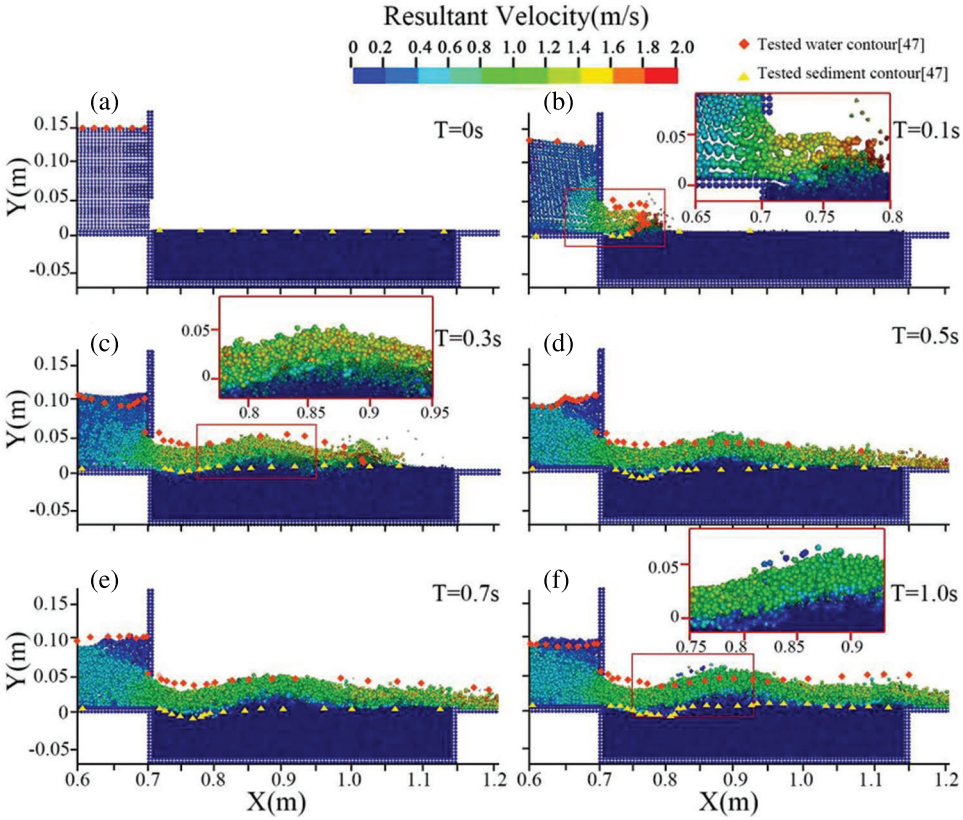

Figure 8: Cloud map of velocity distribution at each time point

In accordance with previous model test results [53], we took the maximum depth of the scour hole D_{final} = 0.02 m as the basis for regularizing the numerical results. Fig. 9 illustrates the dimensionless expression (D/D_{final}) of the scour pit depth D at each time point; the numerical simulation results were observed to be in good agreement with the experimental results. In the early stage of the dam break, the flow violently scours the downstream sand bed, and the scour depth increases rapidly. As water flow is discharged, the change in the scour pit tends to be stable after time = 2 s. Between time = 1 s and time = 2 s, the depth of the scour hole decreases. This decrease is likely because after time = 1 s, reverse free surface waves appear near the gate, driving some bed sand to backfill the hole. More sediment particles are carried by water flow with the intensification of hydraulic scour. The change in the suspended medium concentration affects the physical and mechanical properties of water flow, as well as the final formation of the scour pit [42].

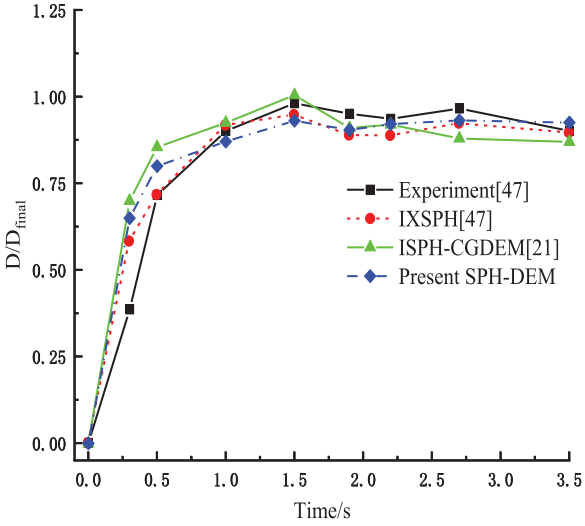

Figure 9: Time history of dimensionless scour hole depth

For the comparison of the scour depth of the one-dimensional angle, the influence of the suspended medium was not obvious. Thus, we considered the erosion analysis of the two-dimensional angle. Fig. 10 shows the time distribution curve of the aspect ratio (D/L) of the scour hole; the dimensionless size distribution of the scour hole calculated by the WCSPH-DEM coupled model lies between the ISPH-CGDEM simulation results and the model experimental results. Hence, the improved strategy of the SPH-DEM coupling model, which uses the fluid mixing viscosity coefficient to characterize the dynamic change in the suspension medium, is effective and feasible. In addition, because of the different solid–liquid coupling control equations selected by each simulation model, some differences exist between the numerical calculations and the experimental observations, but the overall motion change trend is consistent.

3.2 Test 2: Numerical Simulation of Reservoir Sediment Flushing

Another important case analysis in the study of hydraulic soil erosion behavior is the flushing of the bottom sedimentary sand layer by reservoir discharge. We referred to the small-scale flume discharge experiment conducted by Khanpour et al. [53] (see Fig. 5b) to construct an SPH-DEM simulation model for reproducing an idealized reservoir sediment flushing. The initial sketch of the numerical model is shown in Fig. 11. At the beginning, 380000 DEM particles were randomly distributed to fill the sediment layer at the bottom of the tank while 30000 SPH particles were uniformly distributed on the sediment layer with a spacing of 0.01 m. The initial values of the field variables, such as pressure and velocity, were set to zero.

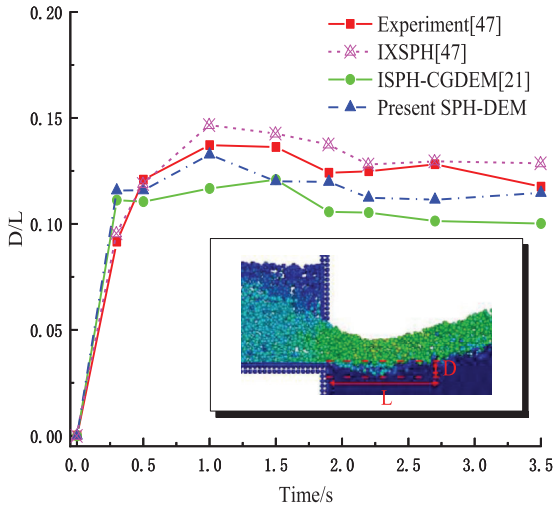

Figure 10: Dimensionless expressions for depth and width scour hole with time

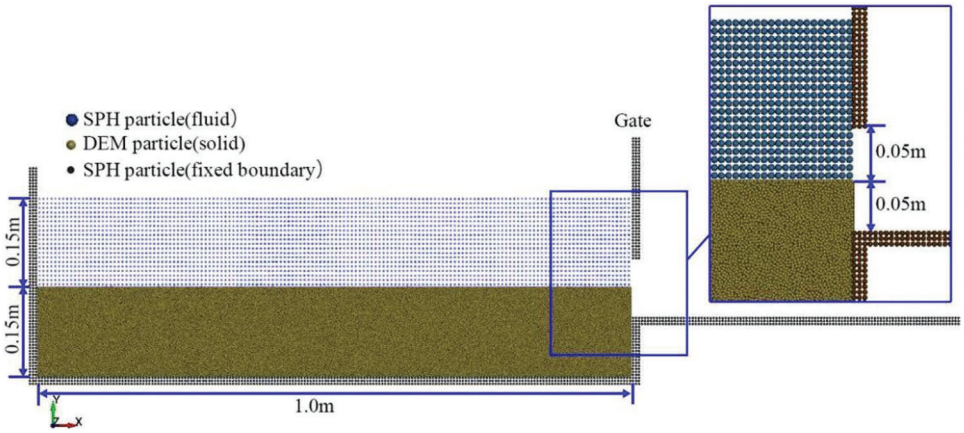

Figure 11: Initial schematic representation of the SPH-DEM numerical model

Fig. 12 illustrates the numerical simulation of the sediment flushing test. As the gate opens, the sediment layer and upper water are released at the same time, discharging the sand-carrying water flow. By tracking and comparing the simulated sediment profile and water level in the flume at different times, we observed that the SPH-DEM numerical calculation results were consistent with the experimental observations.

The output of the velocity distribution nephogram (Fig. 13) indicates that the coupling model completely captures the peak value and corresponding position of the discharge solid–liquid velocity. The fine areas in Figs. 13a–13c show that the erosion effect of SPH particles on DEM particles is significant, and the exposed soil gradually forms a suspended medium layer. On the velocity curve, the difference in velocity between the particles and the liquid is also fully reflected in the bottom precipitation layer because of the damping contact between the DEM particles and SPH particles. Fig. 13d shows that the subsequent movement of the particles is essentially smooth when the suspended media layer disappears and the relative particle velocity approaches zero.

The time distribution curve of the free surface height and sediment thickness at the gate is shown in Fig. 14. When the gate is opened, the water and sand are discharged, and the liquid level peaks quickly. At time = 0.8 s, the sediment thickness fluctuates slightly. By also considering the flow velocity near the

gate (Fig. 13c), we believe that the flow gradually develops from turbulent flow to laminar flow, weakening the relative motion of the solid–liquid interface and thus forming a short-term accumulation of sediment. With time, the height of the free surface gradually decreases, and the flushing effect of water flow on the sediment weakens. After time = 1 s, the change in sediment thickness gradually stabilizes.

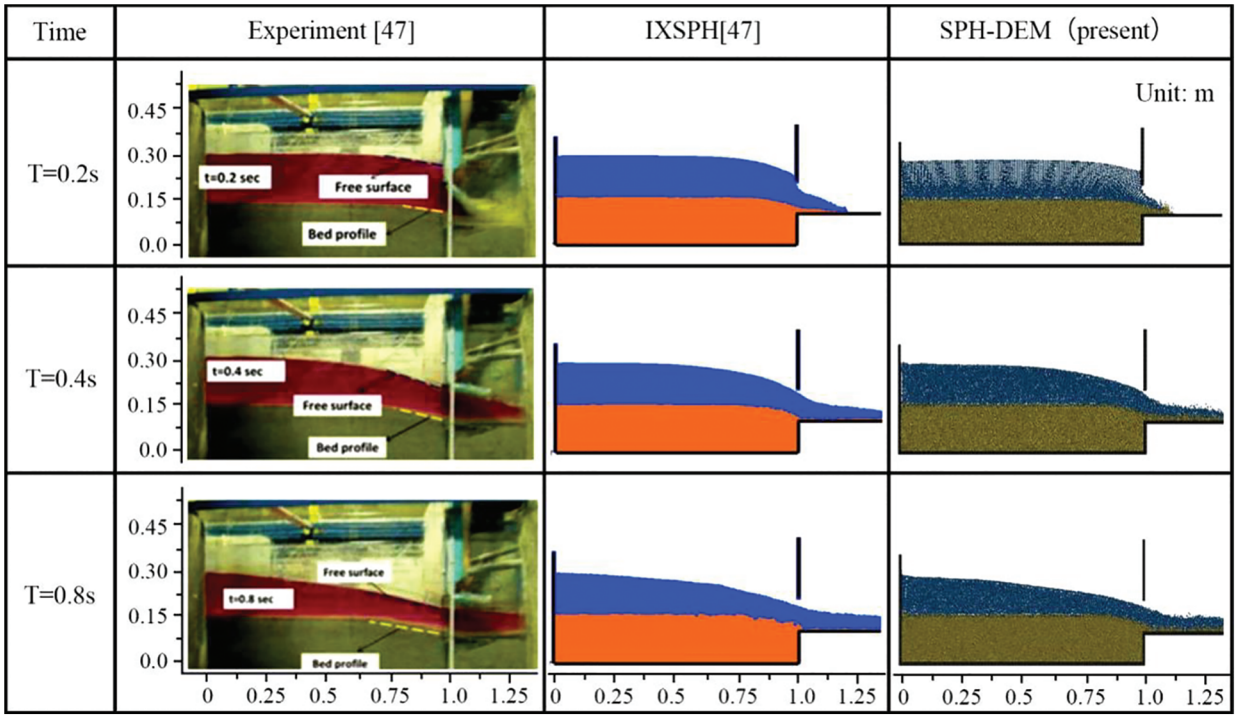

Figure 12: Experimental and numerical results of reservoir sediment flushing test

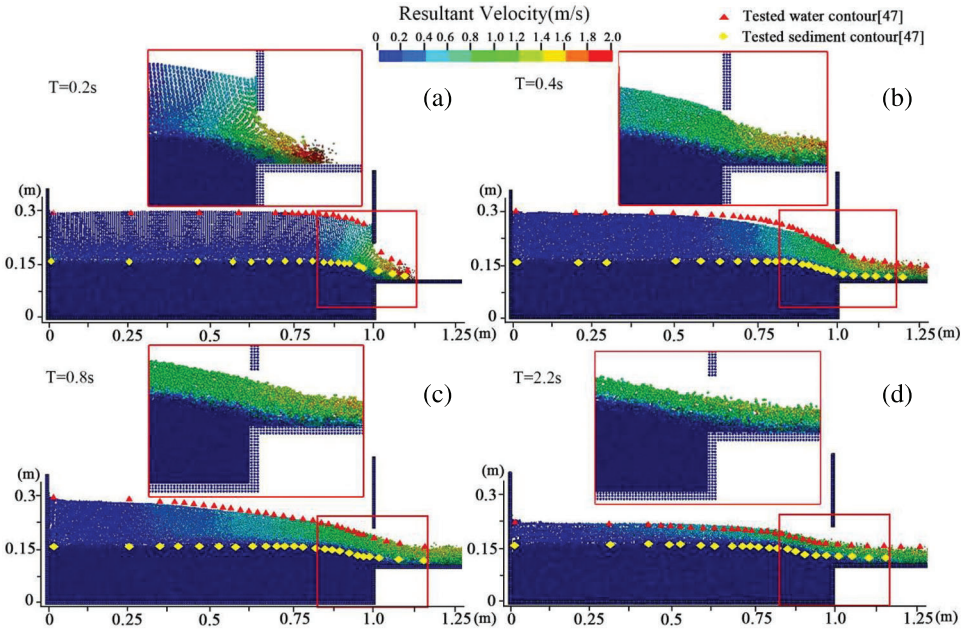

Figure 13: Time history of velocity contour; (a) T = 0.2 s, (b) T = 0.4 s, (c) T = 0.8 s, (d) T = 2.2 s

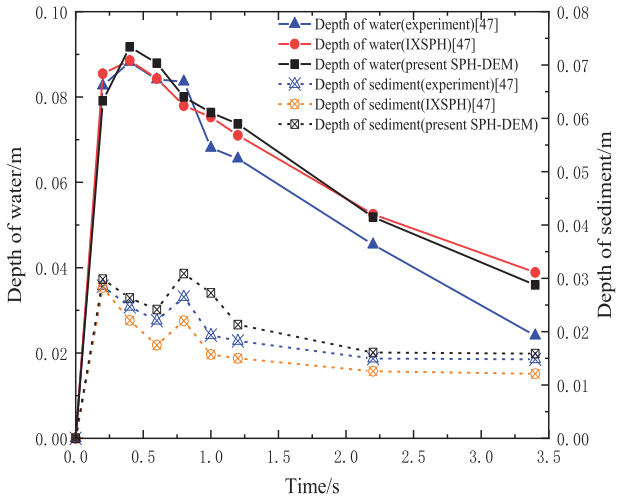

Figure 14: Time history of the water level and sediment thickness at the gate

The scouring efficiency of the sand-carrying flow also needs to be analyzed. The area domain of the graph was determined using AutoCAD software, and the cross-sectional area of the material in the sink at different time nodes was calculated. The volume ratio ($V^{water}/V^{sediment}$) of the cross-sectional unit was obtained from the area ratio, and the flushing efficiency of the water flow was characterized (as illustrated in Fig. 15). The fitting analysis of the volume ratio distribution of the cross-sectional unit shows that the sediment change during the water flushing process (0–3.4 s) satisfies the quadratic equation.

In summary, the two test cases were adequately simulated and reproduced by numerical calculations. The comparison of results shows that our WCSPH-DEM coupling model that considers the influence of a suspended medium is suitable for determining the physical and mechanical parameters in the coupling contact process of a solid–liquid two-phase flow. Therefore, the coupling model is effective for analyzing and solving the problem of hydraulic soil erosion.

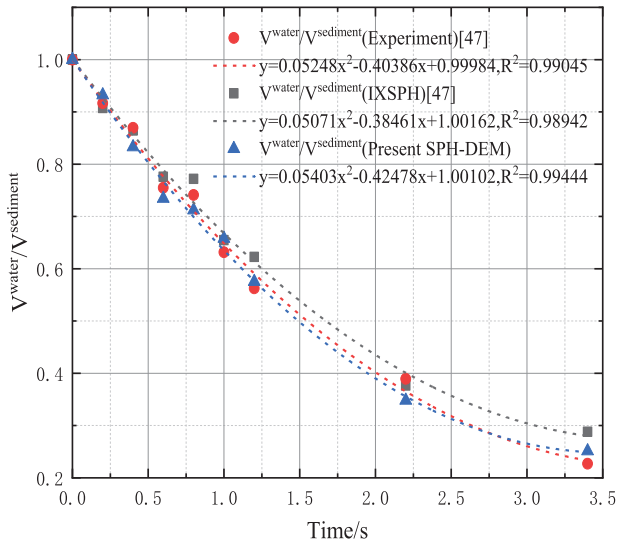

Figure 15: Dimensionless expression of flushing efficiency of the sediment with time

4 Numerical Analysis and Discussion

As earlier mentioned, the suspended medium is an important factor that differentiates between moving bed erosion and clear water erosion, and the suspended mass concentration is the key physical parameter affecting the erosion morphology of the moving bed. We adjusted the sediment thickness at the inlet to analyze the erosion of downstream sediment by sand-carrying flow with different initial concentrations. This approach was selected because of the change in suspended sediment concentration caused by hydraulic soil erosion, as well as the simple and reliable acquisition of the initial viscosity coefficient and the initial sediment volume fraction in the mixed viscosity coefficient, which are the main characterization parameters of the influence of suspended media.

As derived from Eqs. (12) and (13), the sediment erosion is mainly determined by the initial viscosity coefficient of the fluid. When sand-laden flow is used, the influence of the initial sediment content and the initial viscosity coefficient of the flow should be considered [56]. Therefore, we used Case 1 (Section 3) for the simulation model. The relevant material parameters were unchanged, and the sand-carrying flow erosion and clear water flow erosion with different suspended sediment concentrations and flow viscosity coefficients were set, respectively. For the concentration distribution of suspended sediment at the entrance, we used the suspended sediment concentration range of 2456–2700 kg/m^3 (d_{50} = 0.18 mm) [57] in Debnath's test. The sediment density of 2650 kg/m^3 was converted into the initial sediment volume fraction of 0.000927–0.001019. Therefore, 0.001 was selected as the sediment volume fraction of the sand-carrying flow for calculation, and 0.002, 0.003, 0.004, and 0.005 were set for an extended discussion. When the sediment volume fraction of the inlet water flow was 0.001 (the initial water flow depth is 15 cm), the sediment thickness in the storage tank satisfied one layer of DEM particle filling with a median particle size of 0.18 mm. When the gate was opened, the sediment at the bottom collapsed instantaneously, and the initial volume fraction of the sediment met the theoretical setting. By analogy, the settings of other simulation groups met the corresponding sand thickness requirements.

Fig. 16 illustrates the relationship between the initial sediment volume fraction and the local scour depth. As the concentration of suspended sediments in the water flow increases, the peak erosion depth of the water flow to the downstream sand bed gradually increases. However, when the initial sediment concentration reaches 0.004, the peak local scour depth of the downstream sand bed decreases. Chien et al. [31] reported that the increase in sediment thickness is accompanied by an increase in the energy dissipation during sediment transformation from bed load to suspended load, which affects the erosion of suspended sediment flow on the downstream sediment bed. In addition, sediment scours caused by water flow with different initial viscosity coefficients has a strong influence.

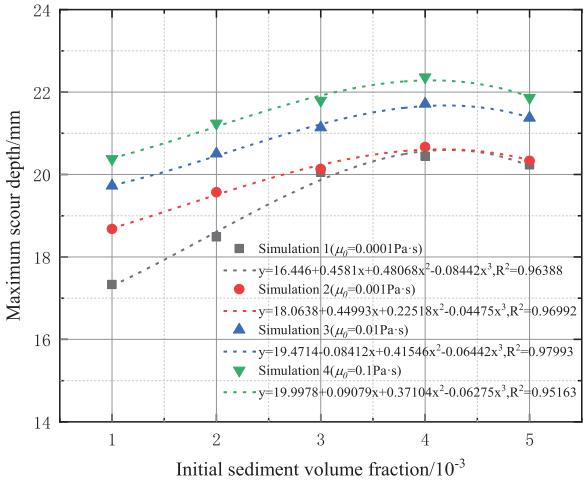

Figure 16: Scour depth peak *vs.* initial sediment volume fraction under different water conditions

Fig. 17 shows the time history curve of the depth of erosion of the downstream bed sand under different suspended sediment concentrations at the entrance of the flume. In the early stage of scouring, the higher the suspended sediment concentration, the smaller the scouring depth. In the later stage of erosion, the higher the suspended sediment concentration, the greater the erosion depth. This behavior occurs mainly because in the two-phase flow model, the existence of suspended load in the initial stage of scouring weakens the turbulent form of water flow. The higher the suspended load concentration, the less obvious the turbulent form of water flow, and the weaker the degree of local scour. In the later stage of erosion development, the presence of suspended sediment increases the viscosity of the sediment-laden flow, increasing the thickness of the laminar layer near the wall, occupying the hydraulic rough area of the hydraulic perimeter, smoothening the perimeter, reducing the reduction of flow velocity or energy loss, and enhancing its ability to scour the riverbed [31]. Comparing clear water erosion (Fig. 9) and sand-carrying flow erosion (Fig. 17), no obvious reverse wave is observed when the suspended sediment flow scours the downstream bed sand, and the change in the scour hole depth does not fluctuate significantly between time = 1 s and time = 2 s.

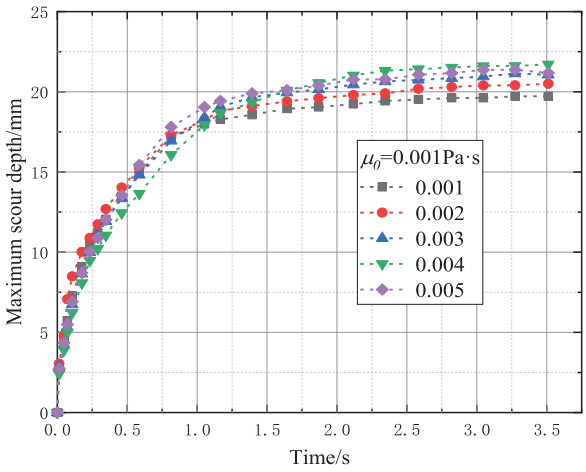

Figure 17: Time history of scour depth peak under different initial sediment volume fractions

We also used the relative error norm (ε_{Yi}) of the scour sand surface elevation (Yi) to evaluate the applicability of each numerical method and model test. ε_{Yi} is expressed as follows:

$$\varepsilon_{Yi} = \sqrt{\sum_{i}^{N} (\delta Y_i)^2 \Big/ \sum_{i}^{N} (Y_i)^2}, \tag{38}$$

where Y represents the model test observation elevation in the scour hole, and δY represents the difference between the numerical calculation results and the experimental observation results in the scour hole. N represents the number of local scour hole depth observations. Table 2 presents the summary of relative error norm of the results under different numerical conditions.

As presented in Table 2, for the case of clear water erosion (Cases 1–3), the relative error of the modified WCSPH-DEM coupling model is smaller than that of the ISPH-CGDEM model, indicating the feasibility of introducing the mixed viscosity coefficient to dynamically characterize the influence of suspended sediment on the flow pattern characteristics. For the influence of the initial viscosity coefficient (Cases 3–6), the error of the numerical calculation results gradually increases with the increase in the initial viscosity coefficient of the water flow. It is reasonable to select $\mu_0 = 0.001$ for the numerical calculation. For the case of scouring sand-carrying water flow (Cases 7–11), the deviation norm of the overall numerical calculation results is

smaller than that of the scouring case of clear water flow (Case 3), indicating that the selection of mixed viscosity coefficients instead of effective viscosity coefficients improves the calculation accuracy of the coupling model.

Table 2: *Yi* relative error norm in calculated elevation of the sediment bed surface

Case	Fluid parameter μ_{mix}		Relative error norm ε_{Yi}	
	Initial sediment volume fraction $\alpha_{s,0}$	Initial viscosity coefficient μ_0		
1	0	0.001	0.0901	IXSPH [47], $\mu_{mix} = \mu_0$
2	0	0.001	0.1479	ISPH-CGDEM [21], $\mu_{mix} = \mu_0$
3	0	0.001	0.1193	Present SPH-DEM, $\mu_{mix} \neq \mu_0$
4	0	0.0001	0.1335	Present SPH-DEM, $\mu_{mix} \neq \mu_0$
5	0	0.01	0.1456	Present SPH-DEM, $\mu_{mix} \neq \mu_0$
6	0	0.1	0.2581	Present SPH-DEM, $\mu_{mix} \neq \mu_0$
7	0.001	0.001	0.0777	Present SPH-DEM, $\mu_{mix} \neq \mu_0$
8	0.002	0.001	0.0909	Present SPH-DEM, $\mu_{mix} \neq \mu_0$
9	0.003	0.001	0.0886	Present SPH-DEM, $\mu_{mix} \neq \mu_0$
10	0.004	0.001	0.1002	Present SPH-DEM, $\mu_{mix} \neq \mu_0$
11	0.005	0.001	0.0924	Present SPH-DEM, $\mu_{mix} \neq \mu_0$

Overall, the occurrence of hydraulic soil erosion depends on the input of initial flow parameters and affects the morphological development of the entire scouring process. The suspended load cannot be ignored in the whole scour analysis, and different concentrations of suspended load can change the characteristics of the scour process.

5 Conclusions

This study aimed to investigate the complex interface between water flow and soil particles in hydraulic soil erosion. A numerical model of hydraulic erosion simulation based on WCSPH-DEM coupling was developed. In the coupling model, the Mohr-Coulomb yield criterion is used for judging whether erosion occurs. The eroded water-sand mixed particles are described with reference to the non-Newtonian fluid characteristics of the Bingham rheological model, and the SPH constitutive control of weakly compressible fluid is established. For the solid part, the DEM particles based on the bond contact relationship adequately track the deformation and failure between the soils. Drag force and buoyancy are introduced to complete the solid-liquid interface processing, and the parallel computing of the WCSPH

method and DEM method is realized. The reliability of the WCSPH-DEM model was verified by comparing its results with those of a wall-jet flushing test and reservoir flushing test [47]. The change in topography, the position of maximum scour depth, and the final topography at an equilibrium scour depth were successfully simulated.

The mixed viscosity coefficient is introduced into the WCSPH-DEM model to characterize the influence of suspended sediment on the dynamic characteristics of soil-water two-phase interface. We analyzed and discussed the effects of initial sediment concentration and initial viscosity coefficient on hydraulic erosion. The local scour depth is positively correlated with the initial sediment concentration and the initial viscosity coefficient, indicating that the suspended medium has a significant effect on the flow pattern and scour pattern of the sand bed. In addition, the comparison of the deviation norm between the calculation results of the different numerical methods and the experimental results further shows that it is feasible to introduce the mixed viscosity coefficient into the proposed model to characterize the influence of the suspended medium on the flow pattern.

However, several problems of the model need to be addressed. For example, the influence of the gap size between discrete particles in the model on the flow needs to be studied and improved. Because of computational resource limitations, the proposed WCSPH-DEM coupling model is two-dimensional. Subsequent research should expand the model to three dimensions using parallel computing or GPU graphics acceleration technology, and the model verification should be conducted through more comparison and quantitative analyses.

Funding Statement: This research was funded by the National Natural Science Foundation of China (No. 51568022) and the Science and Technology Project of Education Department, Jiangxi Province, China (No. GJJ217404).

Conflicts of Interest: The authors declare that they have no conflicts of interest to report regarding the present study.

References

1. Fael, C., Rui, L., Cardoso, A., Engenharia, F. D., Interior, U. et al. (2016). Effect of pier shape and pier alignment on the equilibrium scour depth at single piers. *International Journal of Sediment Research, 31(3),* 244–250.
2. Subhasish, D., Karimbarbhuiya, A. (2006). 3D flow field in a scour hole at a wing-wall abutment. *Journal of Hydraulic Research, 44(1),* 33–50.
3. Garde, R. J., Subramanya, K., Nambudripad, K. D. (1961). Study of scour around spur-dikes. *American Society of Civil Engineers, 87(6),* 23–37.
4. Xue, R., Zhang, X., Cai, Y., Wang, M., Deng, Q. et al. (2021). Numerical simulation of landslide dam overtopping failure considering headward erosion. *Journal of Hydrology, 601,* 1–15.
5. Zhao, Y. B., You, Y., Liu, J. F., Chen, X. C. (2014). Study of gully bed erosion depth of viscous debris flow. *Yantu Lixue/Rock and Soil Mechanics, 35(6),* 1751–1755.
6. Xiong, W., Cai, C. S., Kong, X. (2012). Instrumentation design for bridge scour monitoring using fiber bragg grating sensors. *Applied Optics, 51(5),* 547–557.
7. Ran, Q., Tong, J., Shao, S., Fu, X., Xu, Y. (2015). Incompressible SPH scour model for movable bed dam break flows. *Advances in Water Resources, 82(8),* 39–50.
8. Zhang, Z. L., Walayat, K., Chang, J. Z., Liu, M. B. (2018). Meshfree modeling of a fluid-particle two-phase flow with an improved SPH method. *International Journal for Numerical Methods in Engineering, 116(8),* 530–569.
9. Komoroczi, A., Abe, S., Urai, J. L. (2013). Meshless numerical modeling of brittle-viscous deformation: First results on boudinage and hydrofracturing using a coupling of discrete element method (DEM) andsmoothed particle hydrodynamics (SPH). *Computational Geosciences, 17(2),* 373–390.

10. Cundall, P. A., Strack, O. D. (1979). A discrete numerical model for granular assemblies. *Geotechnique, 29(1),* 47–65.
11. Soodeh, S., Ali, P. (2012). Three-dimensional simulation of fully coupled hydro-mechanical behavior of saturated porous media using the element free galerkin (EFG) method. *Computers and Geotechnics, 46,* 75–83.
12. Bartzke, G., Huhn, K. (2015). A conceptual model of pore-space blockage in mixed sediments using a new numerical approach, with implications for sediment bed stabilization. *Geo-Marine Letters, 35(3),* 189–202.
13. Catalano, E., Chareyre, B., Barthelemy, E. (2014). Pore-scale modeling of fluid-particles interaction and emerging poromechanical effects. *International Journal for Numerical and Analytical Methods in Geomechanics, 38(1),* 51–71.
14. Shamy, U. E., Abdelhamid, Y. (2014). Modeling granular soils liquefaction using coupled lattice boltzmann method and discrete element method. *Soil Dynamics and Earthquake Engineering, 67,* 119–132.
15. Mohammad, N. O., Ali, P., Kenichi, S. (2014). A coupled hydro-mechanical analysis for prediction of hydraulic fracture propagation in saturated porous media using EFG mesh-less method. *Computers and Geotechnics, 55,* 254–266.
16. Blazek, J. (2005). *Computational fluid dynamics: Principles and applications (Second Edition)*. Amsterdam: Elsevier.
17. Zeng, Q. Y., Pan, J. P., Sun, H. Z. (2020). SPH simulation of structures impacted by tailing debris flow and its application to the buffering effect analysis of debris checking dams. *Mathematical Problems in Engineering, 10,* 1–17.
18. Gingold, R. A., Monaghan, J. J. (1977). Smoothed particle hydrodynamics: Theory and application to non spherical stars. *Monthly Notices of the Royal Astronomical Society, 181(3),* 375–389.
19. Aslami, M. H., Rogers, B. D., Stansby, P. K., Bottacin-Busolin, A. (2023). Simulation of floating debris in SPH shallow water flow model with tsunami application. *Advances in Water Resources, 171,* 104363.
20. Bui, H. H., Fukagawar, R. (2013). An improved SPH method for saturated soils and its application to investigate the mechanisms of embankment failure: Case of hydrostatic pore-water pressure. *International Journal for Numerical and Analytical Methods in Geomechanics, 37(1),* 31–50.
21. Dai, Z. L., Huang, Y., Xu, Q. (2019). A hydraulic soil erosion model based on a weakly compressible smoothed particle hydrodynamics method. *Bulletin of Engineering Geology and the Environment, 78(8),* 5853–5864.
22. Ma, X., Zhang, B., Chen, J., Zhou, X. C., Chen, W. (2022). The simulation of sediment transport and erosion caused by free-surface flow based on two-phase SPH model with the improved Shields criterion. *Ocean Dynamics, 72(2),* 169–186.
23. Padova, D. D., Meftah, M. B., Mossa, M., Sibilla, S. (2022). A multi-phase SPH simulation of hydraulic jump oscillations and local scouring processes downstream of bed sills. *Advances in Water Resource, 159,* 104097.
24. Ng, F. C., Zawawi, M. H., Azman, A., Zawawi, M. H., Aziz, N. A. et al. (2022). Smooth particle hydrodynamics modelling of liquid-sediment system and coastal wave breaker. *Ocean Dynamics, 72,* 99–114.
25. Zeng, Q. Y., Zheng, M. X., Huang, D. (2022). Numerical simulation of impact and entrainment behaviors of debris flow by using SPH–DEM–FEM coupling method. *Open Geosciences, 14(1),* 1020–1047.
26. Abbas, Y. B., Hamid, H., Soroush, A. (2020). Lagrangian two-phase flow modeling of scour in front of vertical breakwater. *Coastal Engineering Journal, 62,* 252–266.
27. Iwamoto, T., Nakase, H., Nishiura, D., Sakaguchi, H., Miyamoto, J. et al. (2019). Application of SPH-DEM coupled method to failure simulation of a caisson type composite breakwater during a tsunami. *Soil Dynamics and Earthquake Engineering, 127,* 105806.
28. Kim, J., Lee, J. H., Jang, H., Byun, J., Joo, Y. S. (2021). Numerical investigation of scour by incompressible SPH coupled with coarse-grained DEM. *Soil Dynamics and Earthquake Engineering, 151,* 106998.
29. Han, Z., Bin, S., Yange, L., Wang, W., Wang, W. et al. (2019). Numerical simulation of debris-flow behavior based on the SPH method incorporating the herschel-bulkley-papanastasiou rheology model. *Engineering Geology, 255,* 26–36.

30. Zhang, W., Shi, C., An, Y., Yang, S., Liu, Q. (2019). A viscous elasto-plastic SPH model for long-distance high-speed landslide. *International Journal of Computational Methods, 16(2),* 1846011.
31. Chien, N., Wan, Z. (1999). *Mechanics of sediment transport*. Washington DC, USA: ASCE Publishing.
32. Sun, X. S., Sakai, M., Yamada, Y. (2013). Three-dimensional simulation of a solid-liquid flow by the DEM-SPH method. *Journal of Computational Physics, 248(1),* 147–176.
33. Liu, C., Yu, Z. X., Zhao, S. L. (2021). A coupled SPH-DEM-FEM model for fluid-particle-structure interaction and a case study of Wenjia gully debris flow impact estimation. *Landslides, 18,* 2403–2425.
34. Hosseini, K., Omidvar, P., Kheirkhahan, M., Farzin, S. (2019). Smoothed particle hydrodynamics for the interaction of newtonian and non-newtonian fluids using the μ(I) model. *Powder Technology, 350,* 325–337.
35. Wu, K., Yang, D., Wright, B. N. (2016). A coupled SPH-DEM model for fluid-structure interaction problems with free-surface flow and structural failure. *Computers & Structures, 177,* 141–161.
36. Peng, C., Zhan, L., Wu, W., Zhang, B. (2021). A fully resolved SPH-DEM method for heterogeneous suspensions with arbitrary particle shape. *Powder Technology, 387,* 509–526.
37. Peng, C., Li, S., Wu, W., An, H. C., Chen, X. Q. et al. (2021). On three-dimensional SPH modelling of large-scale landslides. *Canadian Geotechnical Journal, 59(1),* 1–16.
38. Fourtakas, G., Rogers, B. D. (2016). Modelling multi-phase liquid-sediment scour and resuspension induced by rapid flows using smoothed particle hydrodynamics (SPH) accelerated with a graphics processing unit (GPU). *Advances in Water Resources, 92,* 186–199.
39. Rodriguez-Paz, M. X., Bonet, J. (2004). A corrected smooth particle hydrodynamics method for the simulation of debris flows. *Numerical Methods for Partial Differential Equations, 20(1),* 140–163.
40. Papanastasiou, T. C. (1987). Flows of materials with yield. *Journal of Rheology, 31(5),* 385–404.
41. Li, S., Peng, C., Wu, W., Wang, S., Chen, X. Q. et al. (2021). Role of baffle shape on debris flow impact in step-pools channel: An SPH study. *Landslides, 17,* 2099–2111.
42. Vand, V. (1948). Viscosity of solutions and suspensions. I. Theory. *Journal of Physical & Colloid Chemistry, 52(2),* 277–299.
43. Manenti, S., Sibilla, S., Gallati, M., Agate, G., Guandalini, R. (2011). SPH simulation of sediment flushing induced by a rapid water flow. *Journal of Hydraulic Engineering, 138(3),* 272–284.
44. Monaghan, J. J. (1994). Simulating free surface flows with SPH. *Journal of Computational Physics, 110(2),* 399–406.
45. Sakai, M., Koshizuka, S. (2008). Development of a coarse grain simulation methodology for discrete element method in gas-solid flows. *Journal of the Society of Powder Technology Japan, 45(1),* 12–22.
46. Wu, K., Yang, D., Wright, N., Khan, A. (2018). An integrated particle model for fluid–particle–structure interaction problems with free-surface flow and structural failure. *Journal of Fluids and Structures, 76,* 166–184.
47. Robinson, M., Luding, S., Ramaioli, M. (2014). Fluid-particle flow simulations using two-way-coupled mesoscale SPH-DEM and validation. *International Journal of Multiphase Flow, 59,* 121–134.
48. Ergun, S. (1952). Fluid flow through packed columns. *Journal of Materials Science and Chemical Engineering, 48(2),* 89–94.
49. Wen, C. Y., Yu, Y. H. (1966). Mechanics of fluidization. *Chemical Engineering Progress, 62,* 100–110.
50. Brown, P. P., Lawler, D. F. (2003). Sphere drag and settling velocity revisited. *Journal of Environmental Engineering, 129(3),* 222–231.
51. Tsuji, Y., Kawaguchi, T., Anaka, T. (1993). Discrete particle simulation of two-dimensional fluidized bed. *Powder Technology, 77(1),* 79–87.
52. Monaghan, J. J., Kos, A. (1999). Solitary waves on a cretan beach. *Journal of Waterway Port Coastal and Ocean Engineering, 125(3),* 145–155.
53. Khanpour, M., Zarrati, A. R., Kolahdoozan, M., Shakibaeinia, A., Amirshahi, S. M. (2016). Mesh-free SPH modeling of sediment scouring and flushing. *Computers & Fluids, 129,* 67–78.
54. Dai, Z. L., Huang, Y., Cheng, H. L., Xu, Q. (2017). SPH model for fluid-structure interaction and its application to debris flow impact estimation. *Landslides, 14,* 917–928.

55. Bakti, F. P., Kim, M. H., Kim, K. S., Park, J. C. (2016). Comparative study of standard WC-SPH and MPS solvers for free surface academic problems. *International Journal of Offshore and Polar Engineering, 26(3),* 235–243.
56. Xiong, W., Tang, P. B., Kong, B., Cai, C. S. (2017). Computational simulation of live-bed bridge scour considering suspended sediment loads. *Journal of Computing in Civil Engineering, 31(5),* 04017040.
57. Debnath, K., Chaudhuri, S. (2011). Effect of suspended sediment concentration on local scour around cylinder for clay-sand mixed sediment beds. *Engineering Geology, 117(3–4),* 236–245.